Structural, transport, and ultrafast dynamic properties of $V_{1-x}Nb_xO_2$ thin films

Yuhan Wang,[1,2] Jiawei Zhang,[3] Yue Ni,[3] Xinzhong Chen,[3] Ryan Mescall,[3] Tamara Isaacs-Smith,[4] Ryan B. Comes,[4]
Salinporn Kittiwatanakul,[1,5] Stuart A. Wolf,[1,6] Jiwei Lu,[1,*] and Mengkun Liu[3,7,†]

[1]*Department of Materials Science and Engineering, University of Virginia, Charlottesville, Virginia 22904, USA*
[2]*School of Electronic Science and Engineering, Nanjing University, Nanjing 210023, China*
[3]*Department of Physics, Stony Brook University, Stony Brook, New York 11794, USA*
[4]*Department of Physics, Auburn University, Auburn, Alabama 36849, USA*
[5]*Department of Physics, Faculty of Science, Chulalongkorn University, Bangkok 10330, Thailand*
[6]*Department of Physics, University of Virginia, Charlottesville, Virginia 22904, USA*
[7]*Department of Physics, Southern University of Science and Technology, Shenzhen 518055, China*

We report the coherent study of structural, transport, and ultrafast dynamic properties of $V_{1-x}Nb_xO_2$ thin films. Films of a solid solution of $V_{1-x}Nb_xO_2$ ($0 \leqslant x \leqslant 1$) are prepared on (0001) sapphire substrates using reactive target bias ion beam deposition. We found that, at room temperature, the low-temperature lattice symmetry of pure VO_2 (monoclinic, $P2_1/c$) and NbO_2 (tetragonal, $I4_1/a$) is only maintained at low substituting levels ($x < 0.1$ and $x > 0.9$) and regular rutile lattices are adopted by films with higher substituting levels ($0.1 < x < 0.9$). We characterized the dc transport properties and the photoinduced ultrafast dynamics at the terahertz frequency range, both of which demonstrate strong dependence on the film composition. At $x \sim 0.5$, both the dc conductivity and ultrafast response diminish, which corresponds to a strong localization of free charge carriers in the system. The strong composition dependence of film transport, ultrafast dynamic, and insulator-metal transition properties promises approaches to improve the performance of devices based on transition metal oxides.

I. INTRODUCTION

Vanadium dioxide (VO_2) undergoes an insulator-to-metal transition (IMT) from below to above $T_c = 340$ K, accompanied with a structural phase transition from a monoclinic to rutile lattice [1]. The IMT of VO_2 can be characterized by abrupt changes in electrical conductivity and optical transmittance/reflectivity in infrared (IR) and terahertz (THz) regions, making it a suitable candidate for ultrafast switching and optical sensing applications [2–4]. However, the performance of VO_2-based devices inevitably degrades when the operation temperature goes above T_c, which is commonplace in modern electronics. In contrast, NbO_2, a cousin dioxide of VO_2, exhibits IMT at a much higher temperature (~ 1081 K). It is also accompanied with a structural transformation from a body-centered tetragonal (bct) to a regular rutile lattice [5]. As demonstrated by previous limited investigations, NbO_2 also appears to be a good candidate for practical applications such as resistive memories and ultrafast switching using electric bias or optical excitation, especially for high-temperature operations [6–8].

Besides the transition temperature, the IMTs in VO_2 and NbO_2 demonstrate discrepancies in several other aspects. Compared with that of VO_2, the change in electrical conductivity of NbO_2 across IMT upon heating is less abrupt and much smaller in magnitude ($\sim 10^4$ times in VO_2 versus $\sim 10^1$ times in NbO_2) [9–11]. Moreover, for optically induced IMT, ultrafast experiments have demonstrated fast insulator-to-metal switching dynamics in both VO_2 and NbO_2 [8,12–14]. However, in VO_2 the long recovery time from the metallic phase back to the insulator phase has prohibited fast on/off switching applications [15]. Unlike other semiconductors where the recovery time governed by electron-hole recombination process can be modified by forming internal electric field or introducing moderate density of defects [16–18], effective tuning of response time and optical contrast between phases in correlated metal oxides is still lacking. In contrast, recent near-infrared pump-probe [8] and optical pump terahertz probe (OPTP) [14] studies of NbO_2 have shown that the recovery time can be orders of magnitude faster than those of VO_2. However, the photoinduced relative change of near-infrared (800 nm) reflectivity ($\Delta R/R$) and THz conductivity ($\Delta\sigma$) of NbO_2 are much smaller than those of VO_2 [8,14].

Therefore, one may achieve better device performance by alloying these two oxides together (e.g., optical switching with faster recovery rates and larger optical responses). In addition, studying this alloyed system is particularly interesting from the fundamental physical perspective. Both VO_2 and NbO_2 are formed by transition metals in the same column of the Periodic Table, resulting in the commonality of one d valence electron that is not engaged in metal (M)–oxygen (O) bonding. Both of their IMTs at respective critical temperatures are accompanied by structural transformations with similar distortion in the lattice. Thus, the investigation of the alloyed

*jl5tk@virginia.edu
†mengkun.liu@stonybrook.edu
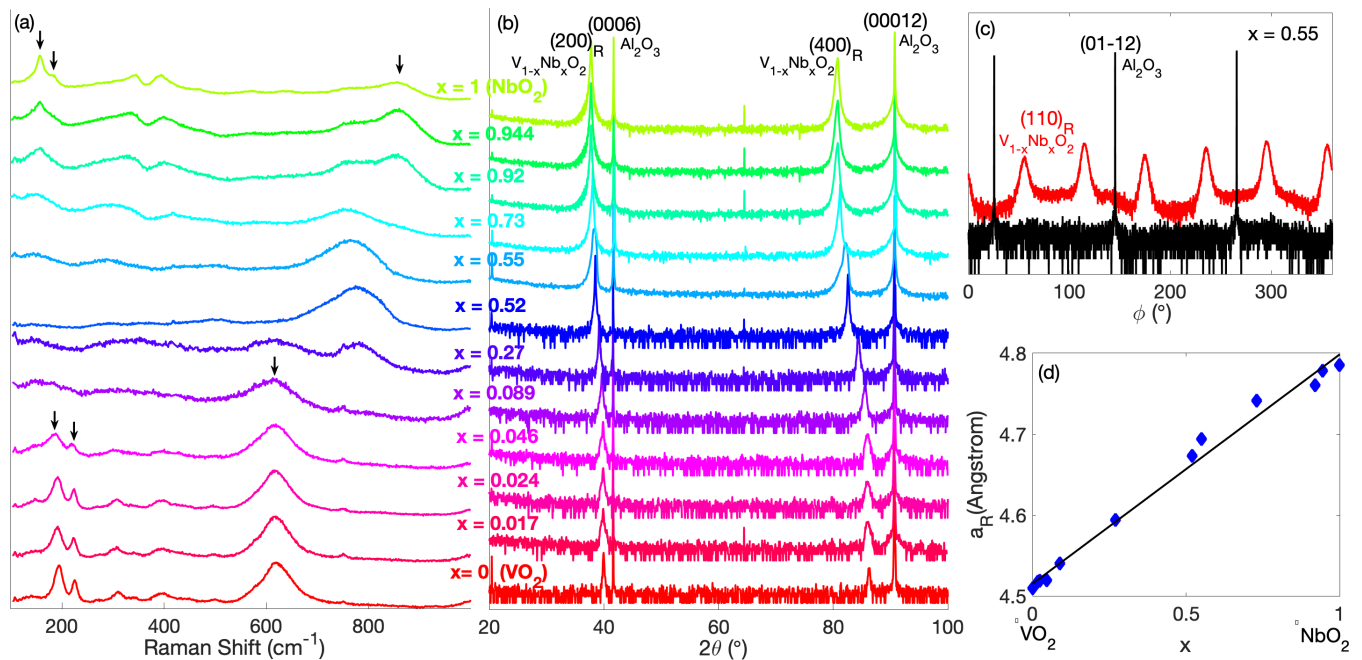
FIG. 1. (a) Raman spectra and (b) X-ray 2θ scans of $V_{1-x}Nb_xO_2$ films. (c) X-ray ϕ scans of (400) diffraction of rutile lattice for the $V_{0.45}Nb_{0.55}O_2$ film at $2\theta = 26°$ and $\chi = 45°$, and $(01\bar{1}2)$ diffraction of sapphire substrate at $2\theta = 25.5°$ and $\chi = 12.8°$. (d) Lattice constant (a_R) as a function of Nb concentration (x).

$V_{1-x}Nb_xO_2$ promises insights into the physics underlying the IMT in d^1 compounds.

II. EXPERIMENT

In this study, we prepare $V_{1-x}Nb_xO_2$ $(0 \leqslant x \leqslant 1)$ thin films by reactive bias target ion beam deposition (RBTIBD) with a full set of x values ranging from 0 to 1. This technique has been employed to prepare high-quality epitaxial VO_2 [19] and NbO_2 [20] thin films on various substrates and its capacity of cosputtering allows for exploration of alloyed material systems [21]. The evolution of lattice structures, dc transport, and photoinduced THz dynamics of the films against composition is systematically investigated.

The $V_{1-x}Nb_xO_2$ thin films are deposited on sapphire (0001) substrates using RBTIBD. Detailed growth conditions can be found in Supplemental Material, Note 1 [22]. The Nb concentration, defined as $x = Nb/[Nb + V]$ (at.%), is measured by Rutherford backscattering (National Electrostatics Corp. Pelletron). The film thicknesses are determined by the x-ray reflectivity (Smartlab, Rigaku Inc.). The film growth rate (nm/min) as a function of composition is plotted in Fig. S1 [22]. X-ray 2θ scans (Smartlab, Rigaku Inc.) are conducted to characterize phase composition, microstructures, and lattice parameters of the films. In addition, x-ray ϕ scans (Smartlab, Rigaku Inc.) are employed to confirm the identification of the 2θ diffraction peaks and to derive the orientation relationship between the $V_{1-x}Nb_xO_2$ films and the substrates. Raman spectra are measured with an inVia Raman spectroscope (Renishaw System Ltd.) using a 514-nm laser source. Temperature dependence of dc resistivity is measured using a VersaLab system (Quantum Design Inc.) from 200 to 400 K with a temperature ramp rate of 5 K/min. For dynamic properties, the static and photoinduced terahertz (0.2–2 THz)

conductivity dynamics are characterized by applying the time-resolved optical pump (800 nm) terahertz probe spectroscopy with a pump power of $\sim 2\,\mathrm{mJ/cm^2}$ (Details in Supplemental Material, Note 2) [22].

III. RESULTS

A. Microstructure

It is known that in their metallic phases, both VO_2 and NbO_2 take a regular rutile lattice $(P4_2/mnm)$ by forming chains of edge-sharing MO_6 octahedra linked at their corners along the c axis. For their semiconducting phases, VO_2 adapts a monoclinic $(P2_1/c)$ lattice and NbO_2 takes a bct $(I4_1/a)$ lattice, sharing essentially the same local deviation from the rutile lattice: formation of $M-M$ dimers along the c axis to yield alternating $M–M$ bond lengths [23–26].

Raman spectra of all the $V_{1-x}Nb_xO_2$ films are shown in Fig. 1(a). Considering their similar lattice structures, it is not surprising that the pure VO_2 and NbO_2 films ($x = 0$ and 1) exhibit similar Raman features, which agrees well with previously reported results [27,28]. For VO_2 the two bands at low frequencies (194 and $225\,\mathrm{cm^{-1}}$) correspond to the stretch and twist modes of the V-V dimers, respectively. The Raman shift near $620\,\mathrm{cm^{-1}}$ in the VO_2 spectrum is related to the symmetric stretching mode of the basal oxygen ions within the VO_6 octahedra [29,30]. Accordingly, for the spectrum of NbO_2 the Raman bands at 158 and $183\,\mathrm{cm^{-1}}$ could be related to the vibration modes of the Nb-Nb dimers caused by the heavier Nb atoms. Moreover, the band near $860\,\mathrm{cm^{-1}}$ could be associated with certain vibration mode within the NbO_6 octahedra.

As the composition moves from pure VO_2 or NbO_2 towards $V_{0.5}Nb_{0.5}O_2$, the two bands related to M-M dimers decrease rapidly in intensity and become absent for samples with
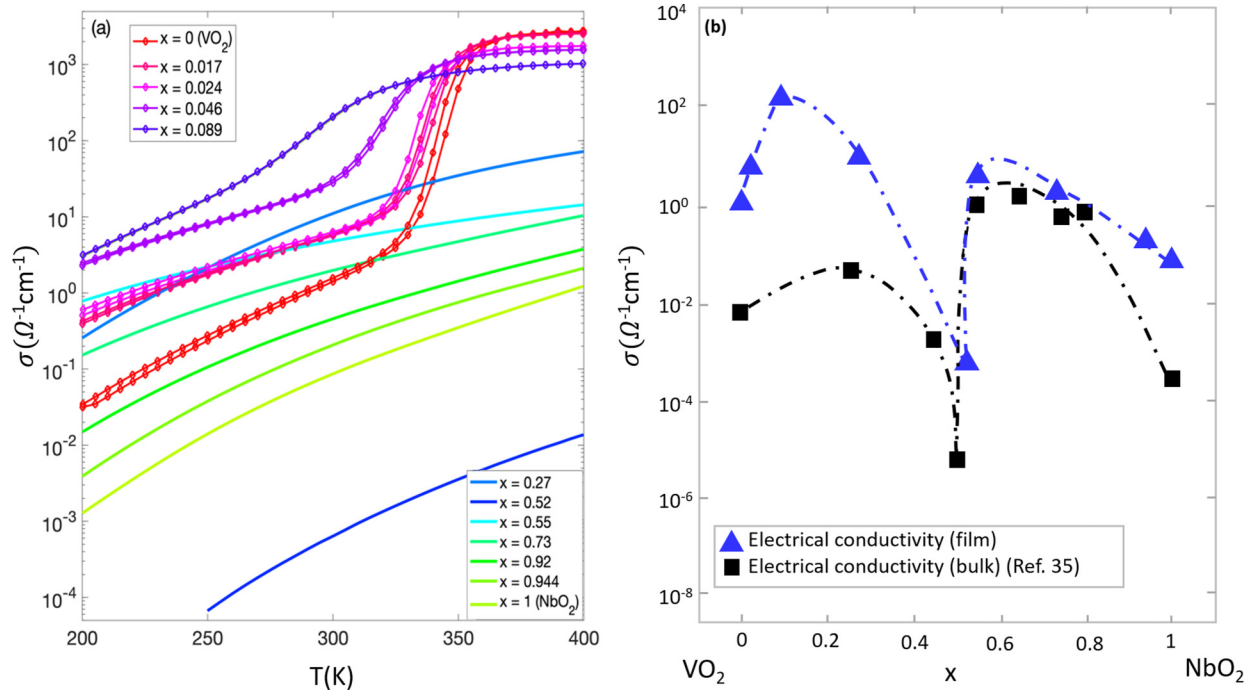
FIG. 2. (a) Temperature dependence of film resistivity in $V_{1-x}Nb_xO_2$ films from 200 to 400 K; (b) Electrical conductivity at $T = 300\,K$ of $V_{1-x}Nb_xO_2$ as a function of Nb concentration (x). The conductivity data of bulk $V_{1-x}Nb_xO_2$ crystals are adapted from Ref. [35].

compositions for $0.089 \leqslant x \leqslant 0.73$. As Nb(V) is substituted into $VO_2(NbO_2)$, it is expected that the $M-M$ dimers will be broken, leading to a decrease in $M-M$ chains tilting along the c axis and the detwisting of MO_6 octahedra. Therefore, there is a transition of the surrounding lattice to a more symmetric, rutile structure [31,32]. The disappearance of the low-frequency Raman features could indicate the collapse of the respective low-temperature symmetry of VO_2 and NbO_2. The broad Raman band developed between 620 and 860 cm^{-1} for samples with composition ranging from $x = 0.27$ to 0.73 is suspected to be related to certain $M-O$ vibration modes within MO_6 octahedra, with the strength of the vibration varied by the $M-O$ bond length and the local distortion of MO_6 octahedra. It is worth noting that no Raman feature of other oxide phases of vanadium or niobium is observed, suggesting that a solid solution has been maintained over the whole range of composition.

Figure 1(b) shows the out-of-plane x-ray 2θ scans of the $V_{1-x}Nb_xO_2$ films, where 2θ is the angle between the incident and diffracted x-ray beams. All samples exhibit diffraction peaks near $2\theta = 40°$ and $2\theta = 86°$. For clarity, all the samples are indexed on the basis of the rutile structure, although the rutile symmetry is distorted when x is close to 0 (VO_2) or 1 (NbO_2). The diffraction peaks correspond to (200) and (400) peaks of the rutile lattice. [For the low-temperature lattices, they correspond to (020) and (040) diffractions of the VO_2 lattice, and (440) and (880) diffractions of the NbO_2 lattice, respectively.] No other diffraction peaks corresponding to any other vanadium-oxide or niobium-oxide phases are present, which further confirms that solid solutions instead of mixed phases are formed over the whole range of composition.

To confirm the assignment of out-of-plane 2θ diffraction peaks, x-ray ϕ (the in-plane orientation of the sample stage)

scans are conducted on (110) diffraction of rutile $V_{1-x}Nb_xO_2$ lattice at $2\theta = 26°$ and $\chi = 45°$ (χ is the tilted angle of the sample stage) based on the lattice symmetry, an example of which is shown in Fig. 1(c) (on the sample with composition $x = 0.55$). Furthermore, the observation of six diffraction peaks, combined with the x-ray ϕ scans of sapphire $(01\bar{1}2)$ diffraction at $2\theta = 25.5°$ and $\chi = 12.8°$, indicates that the orientation relation between the deposited films and substrates is $\langle 001 \rangle (100)_R V_{1-x}Nb_xO_2 \parallel \langle 10\bar{1}0 \rangle (0001)Al_2O_3$. This is the same as that between pure VO_2/NbO_2 films deposited by RBTIBD technique and (0001) sapphire substrates [20,33].

With the increase of x, film peaks shift towards lower 2θ angles, corresponding to an increase of lattice constant along the a axis of the rutile lattice (a_R). In Fig. 1(d), values of a_R are extracted from the 2θ peak positions of $(200)_R$ diffraction and plotted as a function of x, with the black line showing the linear fitting. The increasing trend of a_R with the increase of Nb concentration is due to the larger size of the Nb ion, as the effective ionic radii of V^{4+} and Nb^{4+} in octahedral coordination are 0.58 and 0.68 Å, respectively [34]. In addition, previous studies have pointed out that the Nb (V) substitution introduced into $VO_2(NbO_2)$ would exist as $Nb^{5+}(V^{3+})$, with $V^{3+}(Nb^{5+})$ resulting nearby. This is attributed to the instability of Nb $4d$ electrons compared with that of the V $3d$ electrons [9,35]. The effective ionic radii of V^{3+} and Nb^{5+} in octahedral coordination are both 0.64 Å [34]. Thus the deviation from the linear fitting can be accounted for by the variation in the size of ions.

B. dc transport properties

Figure 2(a) shows the temperature dependence of dc conductivity in all $V_{1-x}Nb_xO_2$ samples from 200 to 400 K. First,
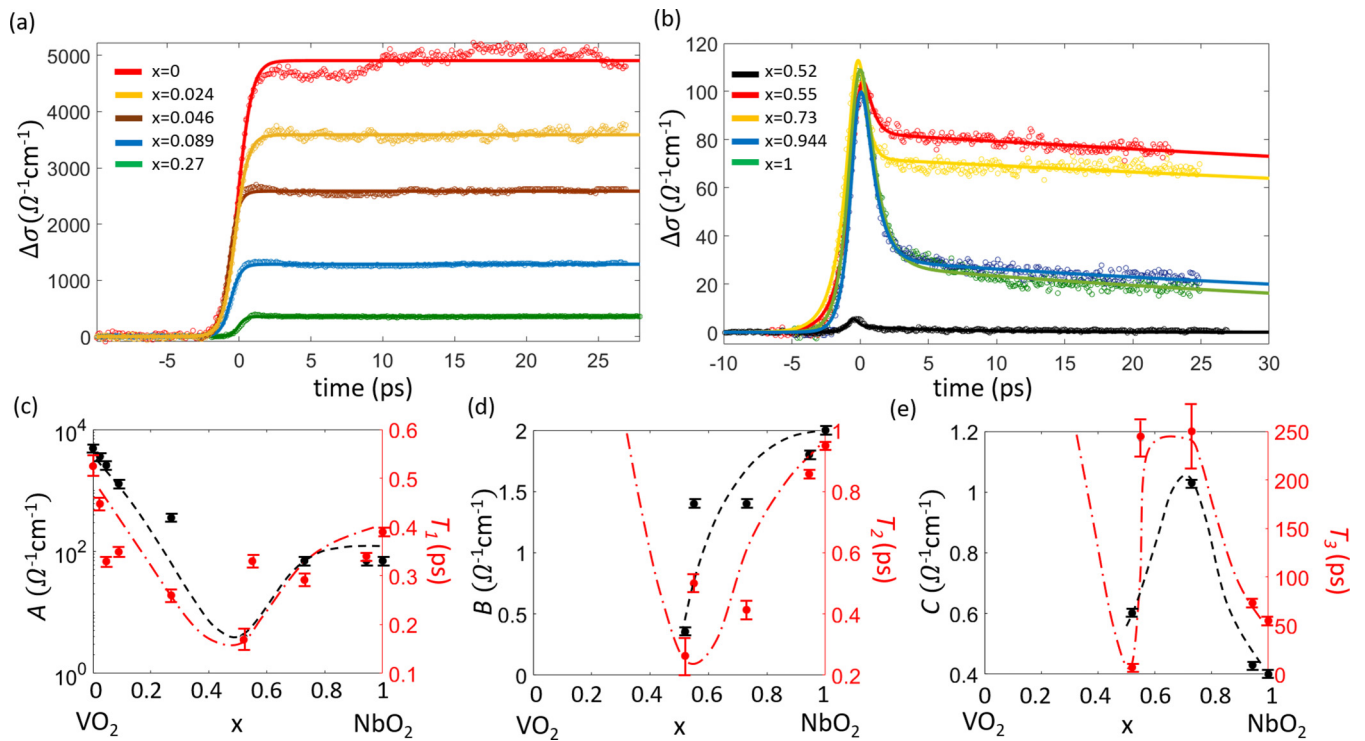
FIG. 3. Optically induced THz photoconductivity change ($\Delta\sigma$) as a function of time for $V_{1-x}Nb_xO_2$ samples with Nb concentration (a) below and (b) above $x = 0.27$. Measurement data are shown in circles while fitting curves in solid lines. (c)–(e) Composition dependence of fitted parameters describing (c) the rise term, (d) the fast decay term, and (e) the slow decay term. The dashed and dashed-dotted curves are guide to the eyes.

samples with Nb concentration up to $x = 0.089$ demonstrate the temperature-driven IMT. With the increase of x, IMT occurs at lower temperatures with smaller and less abrupt changes in the film conductivity across the IMT. The film conductivity of the semiconducting state is enhanced significantly by the Nb substitution, while that of the metallic state only exhibits a slight reduction. As Nb substitution is introduced into VO_2 films, it is expected that the breaking of Peierls distortion and the weakening of electronic correlation within the V-V dimers would result in a decrease of the band gap, leading to the decrease in transition temperature and the increase of conductivity (in the semiconducting phase) [31,36,37]. Similarly, for samples with compositions close to pure $NbO_2(0.92 \leqslant x \leqslant 1)$ which still maintain bct lattices, the conductivity increases as the V substitution level increases.

An interesting observation is that for those samples with intermediate Nb concentration ($0.27 \leqslant x \leqslant 0.73$), the films remain semiconducting despite the observed collapse in monoclinic (bct) symmetry of $VO_2(NbO_2)$. In addition, the film with the composition closest to $V_{0.5}Nb_{0.5}O_2$ (the one $x = 0.52$) exhibits conductivity much lower than all the other samples. The composition dependence of the film conductivity at 300 K is summarized in Fig. 2(b). Similar composition-dependent behavior of conductivity has also been observed in bulk crystals previously [as is shown by the black line in Fig. 2(b)] [35].

C. Ultrafast THz conductivity dynamics

To investigate the effect of cation substitution on the ultrafast dynamics of the $V_{1-x}Nb_xO_2$ samples, time-resolved

THz conductivity dynamics are characterized by OPTP spectroscopy, which are shown in Figs. 3(a) and 3(b). The time resolution of the OPTP measurement is limited by the bandwidth (response time) of the ZnTe detector crystal, which is ~300 fs. As is shown in Fig. 3(a), the samples with Nb content up to $x = 0.27$ demonstrate a long-lived conductivity upon the excitation of the pump pulse, while for other samples with higher Nb concentration the THz dynamics exhibit long-lived but slowly decaying conductivity after the initial fast partial decay [shown in Fig. 3(b)]. The magnitude and lifetime of the photoinduced THz conductivity strongly depend on the film composition.

To quantitatively describe the measured THz conductivity dynamics of these samples, the THz conductivity transient is fitted using the following equation:

$$\Delta\sigma(t) = \frac{A}{1 + e^{-[(t-a)/T_1]}}(Be^{-(t/T_2)} + Ce^{-(t/T_3)}),$$

in which there is one rise term characterized by time T_1 with amplitude A, and two decay terms described by time constant T_2 with amplitude B (fast decay) and time constant T_3 with amplitude C (slow decay), respectively. The composition dependence of these fitted parameters is summarized in Figs. 3(c) to 3(e). First, T_1 and A are both suppressed with the increase of x, reaching a minimum at $x = 0.52$ and then raising at higher Nb concentration, as is shown in Fig. 3(c). For the THz conductivity transients shown in Fig. 3(a), only the rise term ($\frac{A}{1+e^{-[(t-a)/T_1]}}$) is employed in the fitting as negligible decay is observed during the first 30 ps for samples with low Nb concentration. Thus, in Figs. 3(d) and 3(e) the fitted decay

parameters (B, T_2, C, and T_3) are absent for $x \leqslant 0.27$ and only speculated trends are plotted. As shown in Fig. 3(d), the fast decay (for $x > 0.5$) takes place within $\sim$1 ps after the photoexcitation and its magnitude takes an increasing percentage of the maximum photoinduced THz conductivity change as the Nb content increases. Compared with the fast decay, the slow decay term varies more dramatically against composition. The value of T_3 drops from several hundreds of picoseconds to a few tens of picoseconds as the film composition approaches pure NbO$_2$.

It is important to see that the sample $x = 0.52$ exhibits the smallest photoinduced $\Delta\sigma$ [Fig. 3(c)] and fastest "semiconductor-like" decay. This, together with the dc transport data in Fig. 2(b), again suggests the strong localization of carriers in the mixed valent oxide V$_{0.5}$Nb$_{0.5}$O$_2$, even with above-band-gap photoexcitation.

IV. DISCUSSION

A. Semiconducting dc transport behavior of V$_{1-x}$Nb$_x$O$_2$ samples with rutile lattice

VO$_2$ and NbO$_2$ have similar band structures near the Fermi level, which are composed of the π-type overlap between V 3d/Nb 4d and O 2p orbitals with t_{2g} octahedral symmetry determined by the symmetry of MO$_6$ octahedra. In addition, as the MO$_6$ octahedra share edges along the c axis, the orthorhombic symmetry of the crystalline field further degenerates the antibonding π band into the $d_{||}$ and the e_g^π band. For the metallic phase, the $d_{||}$ band overlaps with the e_g^π band with the Fermi level lying in between them. For the semiconducting phase, the $d_{||}$ band is split into the bonding and antibonding band and the e_g^π band is lifted up, giving rising to the band gaps [38–40]. Regarding the origin of the IMT or the nature of the semiconducting phase, for VO$_2$ the dispute centers about the relative contribution from the increased electronic correlation (Mott-Hubbard mechanism) and the metal dimerization (Peierls mechanism) [41–44]. For NbO$_2$ it is generally agreed that the latter should play a more important role due to the larger overlap of 4d orbitals/stronger Nb–Nb bonding [45,46], but electronic correlation also contributes to the band-gap formation, although to a lesser extent, as is revealed by recent density functional theory and cluster-dynamical mean-field calculations [47].

For samples with composition ranging from $x = 0.089$ to 0.73, it is expected that the Peierls insulation is destroyed because of the transformation in lattice structure due to cation substitution. Despite the rutile lattices, the semiconducting transport behaviors could be attributed to the electronic correlation (Mott-Hubbard mechanism) and the enhanced randomness of the film lattice (Anderson localization). A strong enough combination of Coulomb repulsion and lattice disorder could result in the localization of charge carriers and give rise to the observed semiconducting transport behavior [48–50]. In this scenario, the intrinsic electrical conduction could be realized by the electronic hopping of charge carriers. Since the cation substitution results in the formation of Nb^{5+} and V^{3+} in the V$_{1-x}$Nb$_x$O$_2$ system, the real structure of the film would be $V_{1-2x}^{4+}V_x^{3+}Nb_x^{5+}$ for $0 < x < 0.5$ and $V_{1-x}^{3+}Nb_{1-x}^{5+}Nb_{2x-1}^{4+}$ for $0.5 < x < 1$. In principle, the charge-carrier hopping would occur between the same types of cations, manifesting as the position change of cations with the same type but different valences (V^{4+}/V^{3+} or Nb^{5+}/Nb^{4+}). This might explain why the film exhibits conductivity enhancement around the composition where the amounts of V^{3+} and V^{4+} (Nb^{4+} and Nb^{5+}) are close [35,50]. The change in the cations that conduct electricity, combined with the distribution of lattice disorder, could account for the observed variation in the dc transport features against the film composition. At last, the conductivity minimum that occurs at $x \sim 0.5$ can be interpreted as the complete demobilization of conduction carriers due to the valence states V^{3+}/Nb^{5+} [9,35].

B. Ultrafast dynamics of V$_{1-x}$Nb$_x$O$_2$ samples

Since the pump energy (1.55 eV) is well above the band gap of VO$_2$ (0.6–0.7 eV) [51] and NbO$_2$ (indirect band gap of 0.7 eV and direct band gap of 1.24 eV) [46,52], the interband photoexcitation will lead to the generation of a large number of nonequilibrium carriers and thus the rise of THz conductivity. Previous studies of VO$_2$ have shown that when the excitation density (pump fluence) falls below a certain critical value, the full IMT cannot be triggered and the photoinduced carriers relax through various pathways in a few picoseconds, giving rise to the "semiconductor-like" decay features of $\Delta\sigma$ [53,54]. When the excitation density exceeds a certain threshold, the persistence of photoconductivity change indicates that the film has transitioned to a uniform metallic state. It has been reported that the instantaneous modification of electronic correlation by optical excitation could cause subpicosecond band-gap collapse and metal-like optical response, while the establishment of the long-range rutile order may take up to several tens to hundreds of picoseconds [55,56]. Moreover, under certain pump fluence or certain external conditions (such as low temperature), the VO$_2$ films were found to transition to an electronic metallic state while maintaining monoclinic symmetry [53].

Regarding the measured photoinduced THz conductivity dynamics for the V$_{1-x}$Nb$_x$O$_2$ films, the long-lived THz conductivity observed for all the samples (except for the sample $x = 0.52$) indicates that a metastable metallic state is formed by the excitation of the pump pulse. For the samples maintaining the low-temperature lattice of VO$_2$ and NbO$_2$, the absence of a slow increase of the THz conductivity change over a timescale of $\sim$10^2 ps suggests that the full structural transition to rutile lattice has not been triggered [53]. This observation is consistent with other OPTP studies on VO$_2$ and NbO$_2$ films, where the threshold pump fluence to trigger the structural transition is higher than what has been used in our study (2 mJ/cm^2) [14,53]. The metallic response can be attributed to the suppression of the Coulomb repulsion and the resulted collapse of the band gap, which essentially breaks the Mott insulation [43,57,58]. The fast partial decay shown in Fig. 3(b) can be ascribed to the electron-phonon interaction during which the energy is transferred to the lattice. Much shorter processes (within 1 ps) such as electron-electron scattering, localization or self-trapping of photocarriers can also be included [8,59,60]. The slow decay characterized by T_3 can be assigned to the recovery of the metastable metallic

state to the initial semiconducting state, which is faster in Nb-rich samples. The magnitude of THz conductivity change and the recovery rate of the photoinduced metallic state differ more than one order of magnitude across films with different composition, exhibiting strong dependence on the doping concentration. The drastic modulation of the THz conductivity suggests an effective strategy to tailor the dynamic properties of $V_{1-x}Nb_xO_2$ films, which may have practical implication for applications in ultrafast optical switching or memristors with high operation temperature.

V. CONCLUSIONS

In summary, $V_{1-x}Nb_xO_2$ ($0 \leqslant x \leqslant 1$) thin films on sapphire (0001) substrates have been prepared using RBTIBD. Structural characterization demonstrated that the whole system constituted a continuous series of the solid solution and no separated phases were observed. With the increase of cation substitution, the low-temperature lattices of pure VO$_2$ and NbO$_2$ transitioned to more symmetric rutile lattices. Despite the changes in the lattice symmetry, the orientation relationship between the films and substrates remained unchanged by cation substitution as $\langle 001 \rangle (100)_R V_{1-x}Nb_xO_2 \parallel \langle 10\bar{1}0 \rangle (0001)Al_2O_3$. Temperature dependence of dc conductivity was examined from 200 to 400 K and temperature-driven IMT was observed for films with Nb concentration below $x = 0.089$. Films adapting rutile lattices still demonstrated semiconducting electrical transport behaviors across the measured temperature range. Drastic composition dependence of dc transport and ultrafast dynamics properties was observed and an "inert" substituting level at $x \sim 0.5$ was demonstrated to display a lack of both static and photoinduced conductivity. The high tunability of decay time makes $V_{1-x}Nb_xO_2$ a potential candidate for ultrafast optical switches in wire or wireless data transmission.

[1] F. J. Morin, Phys. Rev. Lett. **3**, 34 (1959).

[2] S. Bonora, U. Bortolozzo, S. Residori, R. Balu, and P. Ashrit, Opt. Lett. **35**, 103 (2010).

[3] D. Ruzmetov, K. T. Zawilski, S. D. Senanayake, V. Narayanamurti, and S. Ramanathan, J. Phys.: Condens. Matter. **20**, 465204 (2008).

[4] T. L. Cocker, L. V. Titova, S. Fourmaux, H.-C. Bandulet, D. Brassard, J.-C. Kieffer, M. A. El Khakani, and F. A. Hegmann, Appl. Phys. Lett. **97**, 221905 (2010).

[5] R. Janninck and D. Whitmore, J. Phys. Chem. Solids **27**, 1183 (1966).

[6] S. Kim, J. Park, J. Woo, C. Cho, W. Lee, J. Shin, G. Choi, S. Park, D. Lee, and B. H. Lee *et al.*, Microelectron. Eng. **107**, 33 (2013).

[7] Y. Wang, R. B. Comes, S. A. Wolf, and J. Lu, IEEE J. Electron Devices **4**, 11 (2016).

[8] M. R. Beebe, J. M. Klopf, Y. Wang, S. Kittiwatanakul, J. Lu, S. A. Wolf, and R. A. Lukaszew, Opt. Mater. Express **7**, 213 (2017).

[9] C. N. R. Rao, G. R. Rao, and G. V. S. Rao, J. Solid State Chem. **6**, 340 (1973).

[10] P. Jin, K. Yoshimura, and S. Tanemura, J. Vac. Sci. Technol., A **15**, 1113 (1997).

[11] T. Sakata, K. Sakata, and I. Nishida, Phys. Status Solidi B **20**, K155 (1967).

[12] A. Cavalleri, C. Tóth, C. W. Siders, J. A. Squier, F. Ráksi, P. Forget, and J. C. Kieffer, Phys. Rev. Lett. **87**, 237401 (2001).

[13] M. Liu, H. Y. Hwang, H. Tao, A. C. Strikwerda, K. Fan, G. R. Keiser, A. J. Sternbach, K. G. West, S. Kittiwatanakul, J. Lu *et al.*, Nature (London) **487**, 345 (2012).

[14] R. Rana, J. M. Klopf, J. Grenzer, H. Schneider, M. Helm, and A. Pashkin, Phys. Rev. B **99**, 041102(R) (2019).

[15] H. Wen, L. Guo, E. Barnes, J. H. Lee, D. A. Walko, R. D. Schaller, J. A. Moyer, R. Misra, Y. Li, E. M. Dufresne, D. G. Schlom, V. Gopalan, and J. W. Freeland, Phys. Rev. B **88**, 165424 (2013).

[16] S. Nakamura, Y. Ueno, and K. Tajima, IEEE Photon. Technol. Lett. **10**, 1575 (1998).

[17] A. V. Gopal, H. Yoshida, A. Neogi, N. Georgiev, T. Mozume, T. Simoyama, O. Wada, and H. Ishikawa, IEEE J. Quantum Electron. **38**, 1515 (2002).

[18] W. Kaiser and D. H. Auston, in *Ultrashort Laser Pulses: Generation and Applications*, edited by W. Kaiser (Springer, Berlin, 1993).

[19] K. G. West, J. Lu, J. Yu, D. Kirkwood, W. Chen, Y. Pei, J. Claassen, and S. A. Wolf, J. Vac. Sci. Technol., A **26**, 133 (2008).

[20] Y. Wang, R. B. Comes, S. Kittiwatanakul, S. A. Wolf, and J. Lu, J. Vac. Sci. Technol., A **33**, 021516 (2015).

[21] K. G. West, J. Lu, L. He, D. Kirkwood, W. Chen, T. P. Adl, M. S. Osofsky, S. B. Qadri, R. Hull, and S. A. Wolf, J. Supercond. Novel Magn. **21**, 87 (2008).

[22] See Supplemental Material at http://link.aps.org/supplemental/10.1103/PhysRevB.99.245129 for film growth rate as a function of composition, a description of the film growth conditions, and details on the OPTP measurement.

[23] M. E. A. Warwick and R. Binions, J. Mater. Chem. A **2**, 3275 (2014).

[24] A. Zylbersztejn and N. F. Mott, Phys. Rev. B **11**, 4383 (1975).

[25] A. A. Bolzan, C. Fong, B. J. Kennedy, and C. J. Howard, J. Solid State Chem. **113**, 9 (1994).

[26] A. K. Cheetham and C. N. R. Rao, Acta Crystallogr. B **32**, 1579 (1976).

[27] P. Schilbe, Physica B **316–317**, 600 (2002).

[28] Y. Zhao, Z. Zhang, and Y. Lin, J. Phys. D **37**, 3392 (2004).

[29] A. Cavalleri, T. Dekorsy, H. H. W. Chong, J. C. Kieffer, and R. W. Schoenlein, Phys. Rev. B **70**, 161102(R) (2004).

[30] C. Marini, E. Arcangeletti, D. Di Castro, L. Baldassare, A. Perucchi, S. Lupi, L. Malavasi, L. Boeri, E. Pomjakushina, K. Conder, and P. Postorino, Phys. Rev. B **77**, 235111 (2008).

[31] Y. Wu, L. Fan, Q. Liu, S. Chen, W. Huang, F. Chen, G. Liao, C. Zou, and Z. Wu, Sci. Rep. **5**, 9328 (2015).

[32] Y. Li, Y. Liu, J. Liu, and L. Ren, J. Mater. Sci. Mater. Electron. **27**, 4981 (2016).

[33] J. H. Claassen, J. W. Lu, K. G. West, and S. A. Wolf, Appl. Phys. Lett. **96**, 132102 (2010).

[34] R. D. Shannon, Acta Crystallogr. A **32**, 751 (1976).

[35] H. Oppermann, F. von Woedtke, T. Reich, M. A. Denecke, H. Nitsche, and M. Doerr, Fresen. J. Anal. Chem. **363**, 202 (1999).

[36] Y. Wu, L. Fan, W. Huang, S. Chen, S. Chen, F. Chen, C. Zou, and Z. Wu, Phys. Chem. Chem. Phys. **16**, 17705 (2014).

[37] C. J. Patridge, L. Whittaker, B. Ravel, and S. Banerjee, J. Phys. Chem. C **116**, 3728 (2012).

[38] J. B. Goodenough, J. Phys. Chem. Solids **3**, 490 (1971).

[39] D. Ruzmetov and S. Ramanathan, in *Thin Film Metal-Oxides: Fundamentals and Applications in Electronics and Energy*, edited by S. Ramanathan (Springer, Boston, 2010).

[40] F. J. Wong, N. Hong, and S. Ramanathan, Phys. Rev. B **90**, 115135 (2014).

[41] R. M. Wentzcovitch, W. W. Schulz, and P. B. Allen, Phys. Rev. Lett. **72**, 3389 (1994).

[42] T. M. Rice, H. Launois, and J. P. Pouget, Phys. Rev. Lett. **73**, 3042 (1994).

[43] S. Biermann, A. Poteryaev, A. I. Lichtenstein, and A. Georges, Phys. Rev. Lett. **94**, 026404 (2005).

[44] M. W. Haverkort, Z. Hu, A. Tanaka, W. Reichelt, S. V. Streltsov, M. A. Korotin, V. I. Anisimov, H. H. Hsieh, H.-J. Lin, C. T. Chen, D. I. Khomskii, and L. H. Tjeng, Phys. Rev. Lett. **95**, 196404 (2005).

[45] V. Eyert, Europhys. Lett. **58**, 851 (2002).

[46] A. O'Hara and A. A. Demkov, Phys. Rev. B **91**, 094305 (2015).

[47] W. H. Brito, M. C. O. Aguiar, K. Haule, and G. Kotliar, Phys. Rev. B **96**, 195102 (2017).

[48] N. Mott, in *Metal-Insulator Transitions*, (CRC Press, London/ Bristol, Philadelphia, 2010).

[49] P. W. Anderson, Phys. Rev. **109**, 1492 (1958).

[50] P. Lederer, H. Launois, J. P. Pouget, A. Casalot, and G. Villeneuve, J. Phys. Chem. Solids **33**, 1969 (1972).

[51] M. Rini, Z. Hao, R. W. Schoenlein, C. Giannetti, F. Parmigiani, S. Fourmaux, J. C. Kieffer, A. Fujimori, M. Onoda, S. Wall, and A. Cavalleri, Appl. Phys. Lett. **92**, 181904 (2008).

[52] S. Nakao, H. Kamisaka, Y. Hirose, and T. Hasegawa, Phys. Status Solidi A **214**, 1600604 (2016).

[53] T. L. Cocker, L. V. Titova, S. Fourmaux, G. Holloway, H.-C. Bandulet, D. Brassard, J.-C. Kieffer, M. A. El Khakani, and F. A. Hegmann, Phys. Rev. B **85**, 155120 (2012).

[54] J. Lourembam, A. Srivastava, C. La-o-vorakiat, L. Cheng, T. Venkatesan, and E. E. M. Chia, Sci. Rep. **6**, 25538 (2016).

[55] P. Baum, D.-S. Yang, and A. H. Zewail, Science **318**, 788 (2007).

[56] V. R. Morrison, R. P. Chatelain, K. L. Tiwari, A. Hendaoui, A. Bruhács, M. Chaker, and B. J. Siwick, Science **346**, 445 (2014).

[57] H.-T. Kim, Y. W. Lee, B.-J. Kim, B.-G. Chae, S. J. Yun, K.-Y. Kang, K.-J. Han, K.-J. Yee, and Y.-S. Lim, Phys. Rev. Lett. **97**, 266401 (2006).

[58] T. Yao, X. Zhang, Z. Sun, S. Liu, Y. Huang, Y. Xie, C. Wu, X. Yuan, W. Zhang, Z. Wu, G. Pan, F. Hu, L. Wu, Q. Liu, and S. Wei, Phys. Rev. Lett. **105**, 226405 (2010).

[59] C. Kübler, H. Ehrke, R. Huber, R. Lopez, A. Halabica, R. F. Haglund, and A. Leitenstorfer, Phys. Rev. Lett. **99**, 116401 (2007).

[60] A. Pashkin, C. Kübler, H. Ehrke, R. Lopez, A. Halabica, R. F. Haglund, R. Huber, and A. Leitenstorfer, Phys. Rev. B **83**, 195120 (2011).